UC San Diego
UC San Diego Previously Published Works

Title

An Alongshore Momentum Budget Over a Fringing Tropical Fore-Reef

Authors

Arzeno, Isabella B
Collignon, Audric
Merrifield, Mark
et al.

Key Points:
- A tidal alongshore momentum budget is estimated over a tropical fringing coral reef system
- Unsteadiness, barotropic pressure gradient, and bottom drag play a dominant role on the fore-reef
- Advective acceleration can be of similar magnitude and necessary for budget closure

An Alongshore Momentum Budget Over a Fringing Tropical Fore-Reef

Isabella B. Arzeno[1] iD, Audric Collignon[2], Mark Merrifield[1] iD, Sarah N. Giddings[1] iD, and Geno Pawlak[2] iD

[1] Scripps Institution of Oceanography, UCSD, CA, San Diego, USA, [2] Department of Mechanical and Aerospace Engineering, UCSD, CA, San Diego, USA

Abstract Existing momentum budgets over coral reefs have predominantly focused on cross-reef dynamics, lacking analysis of alongshore processes. To complement existing cross-reef research and enhance our understanding of forcing variability at the semidiurnal period, this study examines the σ – coordinate, depth-averaged alongshore momentum budget over a fore-reef as a function of tidal phase. The observations were gathered over a 3-week timespan, between the 12- and 20-m isobaths of a Hawaiian fringing reef system, focusing on two moorings on the 12-m isobath, where median drag coefficients estimated from log fits are $C_D = 0.0080$ $[-0.002, +0.004]$ and $C_D = 0.0023$ $[-0.0006, +0.0009]$. Analysis at one location shows that the unsteadiness, barotropic pressure gradient, and bottom drag are equally important, and their combination is sufficient to close the momentum budget. However, bottom drag is less important at the second mooring; the difference between unsteadiness and pressure gradient suggests that advective acceleration plays a significant role.

Plain Language Summary Coral reefs are important, productive ocean ecosystems that are highly influenced by hydrodynamic forcing. Although a lot of research has been done to understand what forces drive the flow across tropical reefs (from offshore to onshore), less is known about the forces that drive flow parallel to the shoreline (alongshore). Here we study the physical dynamics over a coral reef in Hawai'i and determine that two primary forces drive the alongshore flow acceleration. One of the dominant forces is the drag exerted by the bottom reef, since coral are rougher than typical sandy coastal beds. The other dominant force is the pressure gradient, associated with the difference in sea level set up by the tide. The tidal cycle and the resulting flow response has important implications for the reef environment, with relevance for reef biology and, eventually, for ecosystem management policies.

1. Introduction

Over the years, the study of physical processes on coral reefs has covered a wide range of relevant scales (Lowe & Falter, 2015; Monismith, 2007). Reef scale hydrodynamics are important for several biological processes including larval dispersal and reef connectivity (Black, 1993; Cowen et al., 2000; Gilg & Hilbish, 2003; Kitheka, 1997; Williams et al., 1984; Wolanski & Kingsford, 2014); they also determine sediment transport and turbidity levels on the reef environment (Douillet et al., 2001; Rogers, 1990). Additionally, reef hydrodynamics have implications on ecosystem management policies (Green et al., 2015). However, to date, the primary focus of reef-scale processes on coral reefs has been on cross-reef dynamics in either non-tidally driven environments or on nontidal timescales.

Significant work has been accomplished, for example, on understanding the cross-shore momentum budget over reefs, particularly wave-driven reefs. The cross-shore momentum budget over a coral reef can often be reduced to a balance that includes the pressure gradient, bottom drag, and/or radiation stress gradients — depending on the reef section under study — while the wind is less influential or negligible (Coronado et al., 2007; Hench et al., 2008; Lentz et al., 2018; Lowe et al., 2009a; Lowe et al., 2010; Monismith, 2014; Taebi et al., 2011). Studies that particularly focus on cross-reef wave-driven flow have shown that waves may impact circulation patterns and residence times in these systems (Coronado et al., 2007; Lowe et al., 2009b), as well as play an important role in enhancing the effects of bottom friction (Grant & Madsen, 1979, 1986) by promoting near-bed momentum transfer and thus intensifying the apparent roughness. A recent study by

Lentz et al. (2018) explores how to properly account for the influence of waves on estimates of bottom drag to improve closure of the cross-reef momentum budget.

Alongshore momentum balances over coral reefs have not been extensively analyzed in the literature. Lentz et al. (2016) study a shallow reef in the Red Sea (1–2 m deep) and assume an alongshore balance between wind stress and bottom stress; however, they find this simplified balance to be lacking some important dynamics. Rogers et al. (2018) briefly looks at the alongshore momentum budget over a shallow pool (1–3 m deep) in Ofu, American Samoa, and determine the main balance to be between the pressure gradient and the bottom drag. Monismith (2014) discusses an alongshore momentum balance over a lagoon by using a simple model and assuming a pressure-friction balance. On the other hand, more extensive research on alongshore momentum budgets over sandy environments does exist, albeit looking at subtidal flows. Fewings and Lentz (2010) and Lentz et al. (1999) suggest that subtidal fluctuations over the inner shelf (approximately 10–15 m deep) are dominated in the alongshore direction by the pressure gradient, wind stress, and bottom stress; nonlinear terms are assumed to be insignificant. Given that estimated values of C_D over coral reefs are typically higher than over sandy substrate — a compilation of C_D from various studies, adjusted to the common definition in Rosman and Hench (2011), show $C_D = 0.01$–0.12 over coral reefs — we expect to find that bottom stress is a dominant term in the alongshore momentum budget over coral reefs, in agreement with previous work.

In this study, we estimate the different terms in the depth-averaged tidal alongshore momentum budget using data from moored instruments on a coral reef off the west coast of Oahu, Hawai'i (Figure 1) at a time when gravity waves are relatively small and wind is weak. Here we (1) quantify terms in the momentum budget, highlighting the four dominant forces and (2) outline how the dynamics change throughout a tidal cycle. Specifically, in section 2, we discuss the observational methods. In section 3, we present the governing equations. In section 4, we outline basic results from our momentum budget estimates and relate them to the tidal phase. Section 5 compares our results with previous studies and discusses the implications. Section 6 summarizes the main results. The appendix includes details on uncertainty calculations and the log fit method used to find the drag coefficient.

2. Methods

Data were collected during September 2013 using an array of moored instruments situated offshore of the west coast of Oahu, Hawai'i (Arzeno et al., 2018). Specific instrument locations are shown in Figure 1. The bathymetry inshore of the 20-m isobath is generally homogeneous on the large-scale but subject to small-scale roughness variability (Figure 2). The root-mean-squared roughness measured by the REMUS autonomous underwater vehicle over a 50m^2 box — root-mean-squared calculations explained in Nunes and Pawlak (2008) — is $O(10^{-3}$ m), higher than sandy substrates but lower than the bottom roughness typical of coral reefs (Jaramillo & Pawlak, 2011; Lentz et al., 2016; Nunes & Pawlak, 2008). The seafloor slope in the cross-shore direction is $O(10^{-2})$.

The mooring array consisted of two bottom-mounted RD Instruments acoustic Doppler current profilers (ADCPs) located 257 m apart at mean depths of 13.6 and 11.9 m, as well as a third ADCP located 274 m offshore of the other two instruments, at a mean depth of 21.8 m. From here on, we will refer to these as the 12mN, 12mS, and 20m ADCPs, based on their locations in Figure 1. The 12- and 20-m ADCPs resolved velocity profiles at vertical intervals of 0.25 and 1.25 m, respectively. All ADCPs were sampling in Mode 12 (fast ping mode) at 0.5 Hz. Thermistor chains were deployed near the 20m and 12mN ADCPs. An acoustic Doppler velocimeter (ADV) was deployed next to the 12mS ADCP (as seen in Figure 2). The ADV sampled at 16 Hz for 12 min every hour. Additionally, two pressure sensors were placed at the northern and southern edges of our sampling site, about 2 km apart in the alongshore direction ($\sim 5°$ from true North), at average depths of 12.2 and 13.6 m, respectively. The wind velocity was not recorded at this site (nor nearby) during the experiment; instead, results from model runs produced at the University of Hawai'i (Y. Chen) with 1.5-km resolution were used. These runs employ the Advanced Research Weather Research and Forecasting (WRF) dynamical solver developed and maintained by the Mesoscale and Microscale Meteorology Division of the National Center for Atmospheric Research. WRF model output has shown good agreement with QuikSCAT measurements, buoy observations, and satellite data (Hitzl et al., 2014; Li & Chen, 2017); however, local winds could be modified by nearby steep mountain topography. For this analysis, we use the hourly wind speed averaged over the nearest two grid points.
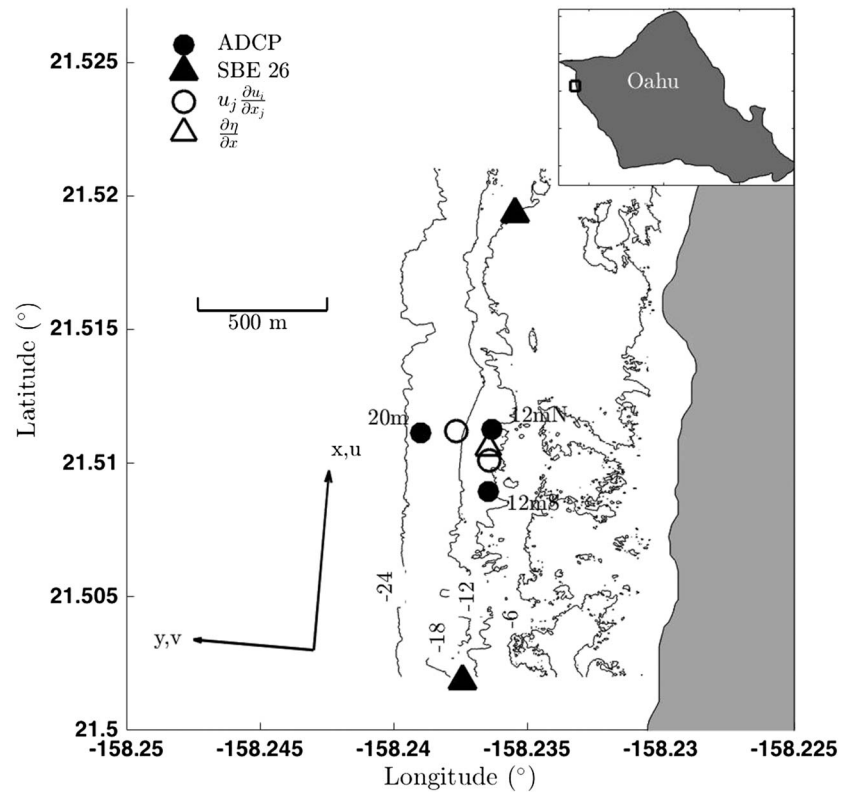
Figure 1. Location of instrument array and estimated momentum budget terms. The inset shows the general study site location on Oahu, Hawai'i. The map bathymetry is taken from SHOALS lidar, with contours depicting the 6, 12, 18, and 24 m depths. ADCP and pressure sensor locations are shown in black shaded dots and triangles, respectively. The approximate location of the advective acceleration estimates are shown as open circles, while that of the barotropic pressure gradient is shown as an open triangle. The along-coast and across-coast coordinate system used in this study is depicted, consistent with the bathymetry. ADCP stands for acoustic Doppler current profiler.

All time series, except for the ADV data, were averaged in 20-min blocks of time wit a 50% overlap. After averaging, the ADCP measurements from the top 15% of the water column were removed, and the velocities were extrapolated assuming no stress at the surface (i.e., no wind), replacing the near-surface data with a constant value equal to the uppermost available velocity. Velocities below the first bin ($\sim$ 1.0 mab) were estimated by extrapolating measurements to the seafloor, assuming a logarithmic profile, applying a no-slip boundary condition. All velocity measurements were interpolated to fall in the same depth bins as those in the northernmost ADCP (12mN). The principal axes for the 12mN, 12mS, and 20m ADCPs are 4.22°, 6.34°, and 1.38° from true North, respectively. The principal axes are not notably different (i.e., vary by less than a degree) if northward and southward velocities are considered separately. However, all velocities were rotated to 5.28°, from true North, roughly parallel to the coastline, in order to facilitate the calculation of gradient terms in the momentum budget. The alongshore and cross-shore directions are denoted by u and v, respectively.

3. Alongshore Momentum Budget

The alongshore momentum budget can be expressed by either a flux-conserving or non-flux-conserving form of the equation. When calculating spatial gradients, the flux-conserving form of the depth-averaged momentum budget (e.g., Lentz et al., 1999) avoids complications due to variations in the bathymetry by taking the spatial derivative of an already depth-integrated velocity product:

$$\frac{1}{D}\frac{\partial}{\partial x_j}\int_{-h}^{\eta} u_i u_j \, dx_3, \tag{1}$$

where $i,j = 1,2$, $D = h + \eta$, h is the mean water depth, η represents the anomalies about h, and u is the depth-dependent velocity. This is in contrast to the non-flux-conserving, depth-averaged form of the
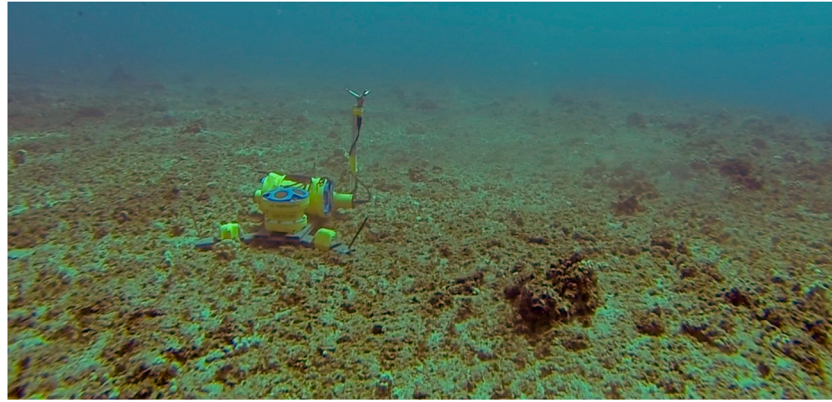
Figure 2. Photo of typical roughness at study site.

momentum equation, where the advective acceleration includes the vertical integral of a term with a spatial derivative:

$$\frac{1}{D}\int_{-h}^{\eta} u_j \frac{\partial u_i}{\partial x_j} dx_3,$$

(2)

and changes in bathymetry become a difficulty. These two forms are interchangeable only when the discretized gradients are centered on the same location, so that continuity is readily satisfied. Given our instrument positions, this assumption does not hold in this study because our cross-shore and alongshore gradients are offset (Figure 1). Since horizontal continuity, in its discretized form, is not zero for this study, that is,

$$u\frac{\partial u}{\partial x} + u\frac{\partial v}{\partial y} \neq 0,$$

(3)

and since we cannot calculate $u\frac{\partial w}{\partial z}$, the advective acceleration terms estimated in flux-conserving form (definition 1) yield values that are almost twice as large as the advective acceleration in the non-flux-conserving form (definition 2).

Thus, in order to minimize uncertainty in the advective acceleration, we choose to analyze the momentum budget using the non-flux-conserving form of the equation in depth-normalized coordinates, to accommodate any general bathymetric changes between instruments that may affect gradient calculations — such as the depth difference between the 12mN and 12mS moorings — when estimating the alongshore advective acceleration. Following Giddings et al. (2014), the depth-averaged, depth-normalized momentum equation, assuming hydrostatic conditions and $\eta \ll D$, can be described by

$$\underbrace{\frac{\partial U_i}{\partial t}}_{1} + \underbrace{\int_0^1 u_j \frac{\partial u_i}{\partial x_j} d\sigma - \frac{\sigma}{D}\left(\int_0^1 \frac{\partial u_i}{\partial \sigma}\left(u_j\frac{\partial D}{\partial x_j} + \frac{\partial D}{\partial t}\right)d\sigma\right) + \int_0^1 \frac{w}{D}\frac{\partial u_i}{\partial \sigma}d\sigma}_{2} + \frac{1}{D}\int_0^1 \frac{\partial\left\langle u_i' u_j'\right\rangle}{\partial x_j}d\sigma + 2\epsilon_{ijk}\Omega_j U_k$$

$$= \underbrace{-g\frac{\partial \eta}{\partial x_i}}_{3} - \frac{gD}{\rho_0}\frac{\partial}{\partial x_i}\int_0^1\int_\sigma^1 \rho\, d\sigma d\sigma + \frac{g}{\rho_0}\frac{\partial D}{\partial x_i}\int_0^1\int_\sigma^1 \sigma\frac{\partial\rho}{\partial\sigma}d\sigma d\sigma - \underbrace{\frac{1}{D\rho_0}(\tau_b - \tau_s)}_{4},$$

(4)

where $i,j = 1, 2$, $\sigma = \frac{z}{D}$ (with $D = h + \eta$, where h is the mean water depth and η represents the anomalies about h), u_i is the depth-dependent velocity, $U_i = \int_0^1 u_i d\sigma$, and τ_s and τ_b are the surface and bottom stresses, respectively. All variables are 20-min averages, except for u_i', the deviations from the average (both wave and turbulence-induced fluctuations). Brackets $\langle\rangle$ denote the time average of the nonlinear deviation terms.

The unsteadiness, advective acceleration, barotropic pressure gradient, and bottom stress are highlighted, in order, by the numbers 1–4.

The σ-coordinate advective acceleration was discretized as

$$u_j \frac{\partial u_i}{\partial x_j} = \overline{u_j} \frac{\Delta u_i}{\Delta x_j}, \tag{5}$$

where $\overline{u_j}$ is the spatial average of the velocities. The sea surface displacement η is the deviation from the time mean pressure at each location, and the barotropic pressure gradient was calculated as the difference in sea surface displacement between the locations of our pressure gauges, assuming that there are no steady gradients on the timescale of the deployment. Thus, the discretized terms are not exactly at the same location (see Figure 1), but they are all within 150 m of the 12mN ADCP. The wind stress τ_s was parameterized using a typical quadratic drag law

$$\tau_s = \rho_a C_D U_i^w \sqrt{U_j^w U_j^w}, \tag{6}$$

where $i = 1, 2$, $\rho_a = 1.2$ kg m^{-3} is air density, U_i^w is wind velocity, and C_D for the wind stress is taken to be $C_D = 1.1 \times 10^{-3}$, according to Smith (1988). The bottom stress τ_b was estimated following

$$u_* = \sqrt{\frac{\tau_b}{\rho}}, \tag{7}$$

where u_* is the shear velocity in the alongshore direction. The shear velocity was found by fitting the boundary layer velocity to a log-law and defect-law profile.

If the velocity observations follow a log-law and defect-law profile, given a steady, fully developed flow, our mean vertical velocity profile can be described as

$$\langle u \rangle = \frac{u_*}{\kappa} \left\{ \ln \left(\frac{z - z_{\text{ref}}}{z_0} \right) + 2\Pi \sin^2 \left[\frac{\pi (z - z_{\text{ref}})}{2\delta} \right] \right\}, \tag{8}$$

where $\kappa = 0.41$ is the Von Kármán constant, z_{ref} is a reference height for the velocity profile, z_0 is a roughness length scale, $\Pi = 0.2$ is Coles' wake strength parameter for high Reynolds number flows (Coles, 1956; Nezu & Rodi, 1986), and δ is the boundary layer height, taken to be the last bin in the log fit, following Rosman and Hench (2011). (Details on the log fit method are described in Appendix A.) In addition, drag estimates from log fits were compared to those from independent calculations (not shown here) using cospectral fits from ADV and ADCP data (Gerbi et al., 2008; Kirincich & Rosman, 2011; Kirincich et al., 2010). The drag coefficients estimated using these three methods fall within error bars of each other.

The drag coefficient is defined from the values of shear velocity, following Lentz et al. (2018), as

$$C_D = \left(\frac{u_*}{\left\langle \int_0^1 u_i d\sigma \int_0^1 \sqrt{u_j u_j} d\sigma \right\rangle} \right)^2, \tag{9}$$

where $i = 1, 2$, u_i is the full (not time-averaged) velocity, and the brackets $\langle \rangle$ denote the 20-min time averaging. Although Lentz et al. (2017) and McDonald et al. (2006) note that the depth-averaged drag coefficient (C_D) generally depends on the ratio of total water depth (D) to roughness length scale (z_0), they also observe that, excluding waves, $C_D \to 0.01$ as the ratio of D to z_0 increases. In particular, Lentz et al. (2017) indicate that C_D asymptotes for $\frac{D}{z_0} > 100$, which we will argue in section 5 to be the general case for our study site.

4. Overview of Results

General observations show that the semidiurnal tidal signal dominates the pressure fluctuations (Figure 3a), with a pronounced diurnal inequality and fortnightly cycle. The tidal range reached a maximum of ~0.55 m during our sampling period. Output from the WRF model runs shows that the wind was predominantly in the
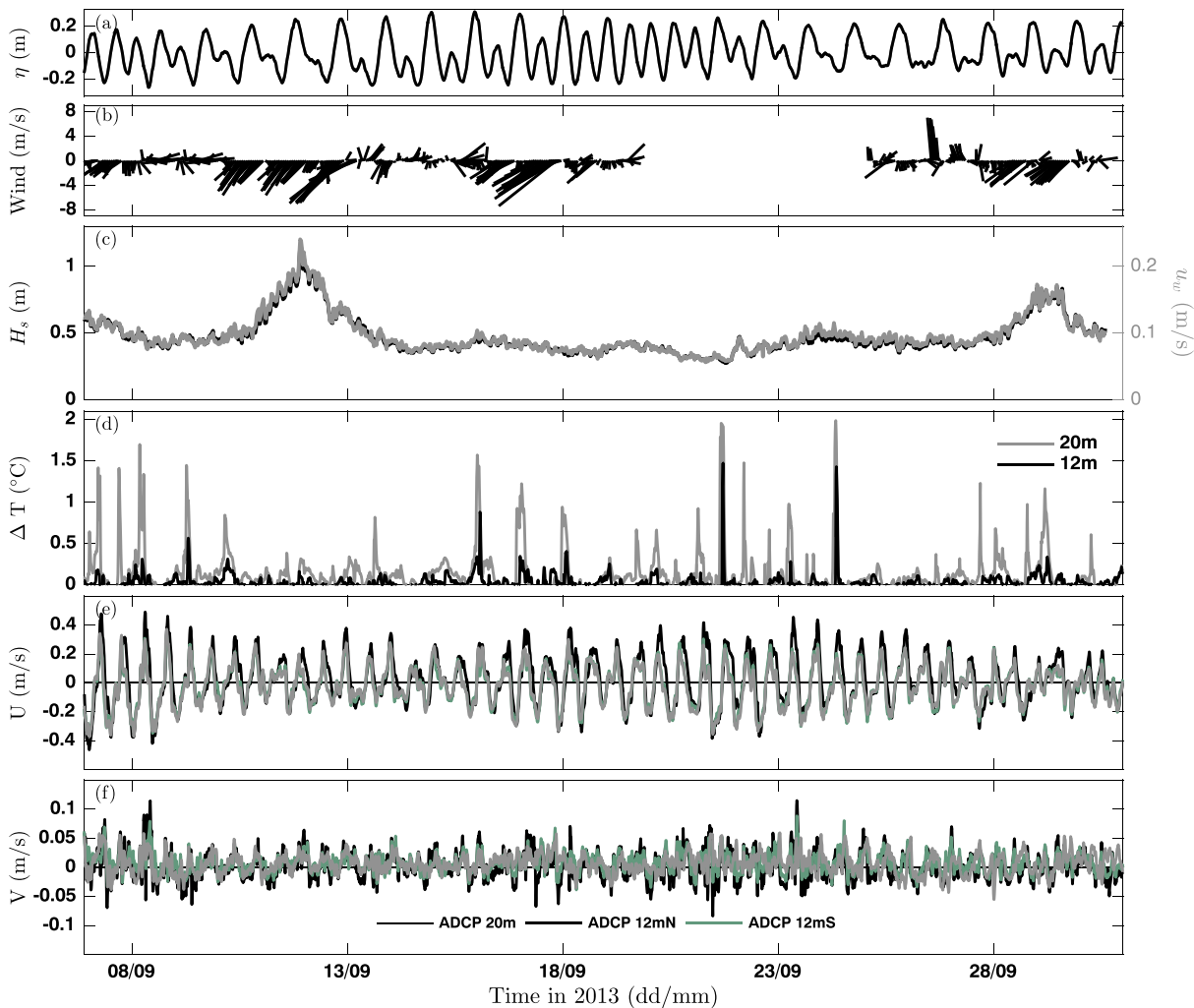
Figure 3. (a) Time series of sea surface displacement at the northern pressure sensor, (b) model output wind velocity near the study site, (c) wave height and bottom wave orbital velocity from spectral analysis and linear theory, (d) difference in temperature between top and bottom thermistors at the 12mN and 20m mooring sites, and (e) alongshore and (f) cross-shore depth-averaged velocities (each defined in section 2).

southwest direction during the observational period (Figure 3b) at an absolute speed less than 12 m/s. Significant wave heights (H_s) calculated using spectral analysis and linear wave theory were, on average, $H_s = 0.40$ m and $H_s = 0.50$ m at the northern and southern pressure sensor locations, respectively, with a maximum of ~1.2 m during a period of swell (Figure 3c). (There were not enough effective degrees of freedom to properly calculate 95% confidence intervals for the mean H_s.) The near-bottom wave orbital velocities (Figure 3c) are the same order of magnitude as the alongshore depth-averaged velocities (Figure 3e).

The temperature difference (ΔT) between the top and bottom sensors on the thermistor chain (1.12 m below the surface and 0.30 m above the bottom) at the 12-m isobath was, on average, $\overline{\Delta T} = 0.34 \pm 0.0025$ °C (Figure 3d). Salinity was only measured on the 12m mooring, near the bottom, and varied little over the observational period (mean of 35.33 ± 0.006 psu). For calculations of the Brunt Väisälä frequency (N^2), we apply this bottom salinity time series over the entire water column, recognizing that it may result in an underestimate of the stratification. In general, our estimated Brunt Väisälä frequencies are low and only rise above the Coriolis frequency in 8.3% and 26.8% of the vertical profiles from the 12mN and 20m moorings, respectively. Intermittent sharp changes in temperature are seen near the bottom of the 20m thermistor chain and are likely associated with shoaling internal waves. Overall, we consider the system to be weakly stratified. Richardson numbers (calculated at every depth where stratification could be estimated) were below the critical value of $Ri = 0.25$ (throughout the entire water column) over 99% and 95% of the sampling time at the 12mN and 20m

Table 1
Median Values of Log Fit Parameters Taken From the Entire Time Series

	12mN	12mS
% with $R^2 \geq 0.95$	72%	53%
u_* (m/s)	0.015 ± 0.002	0.0095 ± 0.0013
z_0 (m)	0.11 ± 0.04	0.0032 ± 0.003
z_{ref} (m)	$0\ [-0, +0.01]$	$0\ [-0, +0.003]$
δ (m)	3.47 ± 0	3.76 ± 0
C_D	$0.0080\ [-0.002, +0.004]$	$0.0023\ [-0.0006, +0.0009]$
C_D^+	$0.0068\ [-0.002, +0.004]$	$0.0017\ [-0.0006, +0.0008]$
C_D^-	0.0090 ± 0.003	$0.0026\ [-0.0007, +0.0009]$

Note. The asymmetric confidence intervals result from using bootstrap methods.
$^+$Drag coefficients calculated using positive alongshore, depth-averaged velocities.
$^-$Drag coefficients calculated using negative alongshore, depth-averaged velocities.

offshore moorings, respectively, indicating that our sampling location is mostly vertically well mixed. When performing logarithmic fits to estimate drag coefficients, we exclude any observations where $Ri > 0.25$.

Alongshelf current variability is dominated across the water column by the semidiurnal tidal cycle (Figure 3e), and depth-averaged currents are incoherent (not phase locked) with the surface pressure at the semidiurnal frequency (Figure 3a). This will be discussed further in section 5. The depth-averaged M_2 tidal ellipses at the 12m moorings account for over 60% of the total variance and are oriented in the alongshore direction. Standard deviations for the depth-averaged alongshore tidal velocities at the three moorings were $\sigma = 0.14$–0.17 m/s (Figure 3e). Cross-shelf currents were significantly weaker than those in the alongshelf direction; their standard deviations were an order of magnitude smaller than those for the alongshore velocities. The largest standard deviation in the cross-shelf currents was $\sigma = 0.023$ m/s, at the 20m ADCP (Figure 3f).

4.1. Drag Estimates

Drag coefficients were estimated using the resulting u_* from the log fits, following equation (9). In general, we found better fits for the 12mN velocity profiles, with 72% of the fits having $R^2 \geq 0.95$, while only 53% of the fits had $R^2 \geq 0.95$ at 12mS. The median value for C_D at the 12mN mooring is $C_D = 0.0080\ [-0.002, +0.004]$; at 12mS, $C_D = 0.0023\ [-0.0006, +0.0009]$. (The confidence intervals were computed by bootstrapping, which sometimes result in asymmetric uncertainties.) As mentioned previously, drag coefficient values from the log fits at 12mS were confirmed with two additional estimates using cospectral fits applied to velocities from both the ADV (Gerbi et al., 2008) and the ADCP (Kirincich & Rosman, 2011; Kirincich et al., 2010).

In general, drag at this site is weaker than what has been previously reported for other tropical coral reefs (e.g., Rosman & Hench, 2011), likely because of the study region's relatively low roughness (refer to Figure 2). There are spatial differences within the study region: the median C_D and z_0 are statistically significantly lower at 12mS than at 12mN. The values are not heavily influenced by current directionality: Estimating different C_D for positive and negative alongshore velocities results in median values with overlapping confidence intervals. There is a statistically significant difference in C_D values estimated for northward and southward velocities only at the 12mS mooring when we consider the largest 25% of the velocities ($|U| > 0.17$ m/s). The current directionality did affect the fit profiles; a larger percentage of log fits met our quality standards when the depth-averaged alongshore velocities were directed southward (77% at 12mN and 63% at 12mS) rather than northward (66% at 12mN and 41% at 12mS).

The statistics of the various parameters in equation (8) are presented in Tables 1 and C1 for the 12m moorings. For the purposes of estimating a bottom stress to include in our momentum budget calculations, we choose to use the time-varying results of the log fits (not the statistical averages) for added accuracy, given that drag coefficient can be a function of the wave-current velocity ratio, although tidal phase averages of C_D do not vary significantly over a tidal cycle. Further, we do not consider the 20m ADCP in our analysis because only a small fraction of the log profiles met our quality standard, likely because the 20m ADCP sampling scheme averaged to a lower vertical resolution than that for the 12m moorings.
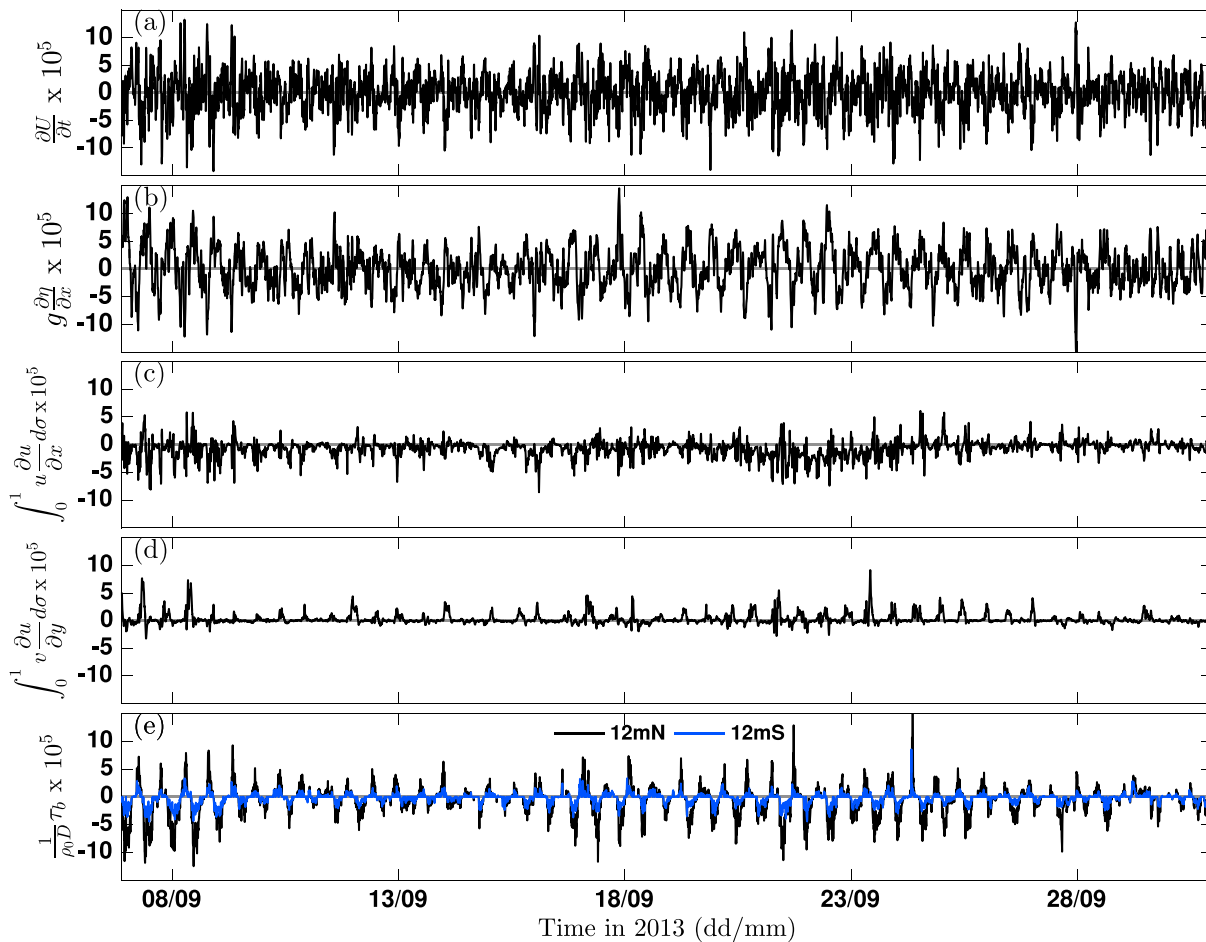
Figure 4. Dominant terms in the momentum budget (m/s^2), multiplied by a factor of 10^5. (a) Depth-averaged unsteadiness $\left(\frac{\partial U}{\partial t}\right)$ at 12mN; (b) barotropic pressure gradient $\left(g\frac{\partial \eta}{\partial x}\right)$; (c) depth-averaged alongshore advective acceleration $\left(\int_0^1 u\frac{\partial u}{\partial x}d\sigma\right)$; (d) depth-averaged cross-shore advective acceleration $\left(\int_0^1 v\frac{\partial u}{\partial y}d\sigma\right)$; (e) bottom drag $\left(\frac{1}{\rho_0 D}\tau_b\right)$ at 12mN and 12mS. The depth-averaged unsteadiness at 12mS has been omitted for graphic clarity, given its similarity to that at 12mN. The 95% confidence intervals have been omitted, since their size (2 to 3 orders of magnitude smaller than the terms) renders them difficult to observe in this plot.

4.2. Momentum Balance

The largest terms in the momentum budget at both 12m moorings are the unsteadiness, barotropic pressure gradient, advective acceleration, and bottom stress (estimated using a time-varying drag coefficient), with magnitudes $O\left(10^{-5}\right)$. These components are numbered in equation (4), and their time variability is presented in Figure 4, with 95% uncertainty intervals calculated using error propagation, as explained in Appendix B. Specifically, the unsteadiness and barotropic pressure gradient terms dominate the momentum budget at both 12m moorings (Figures 4a and 4b). The bottom stress magnitude at 12mN is comparable to that of the unsteadiness and pressure gradient; however, bottom stress is significantly smaller at 12mS (Figure 4e). The advective acceleration could be an important contributor during certain tidal phases, particularly at 12mS, where the bottom drag is weak. The alongshore component of the advective acceleration is mostly negative, while the cross-shore component is positive (Figures 4c and 4d), resulting in mean values $O(10^{-5})$ (Table 2). This suggests that a net momentum flux is possible. However, the instrument array may not be dense enough to accurately capture the advective acceleration during the entire tidal cycle. These five terms fluctuate with a semidiurnal frequency, increasing and decreasing with a fortnightly cycle.

The wind stress, Coriolis force, and the remaining, resolvable nonlinear terms are all, at least, an order of magnitude smaller than the numbered terms in equation (4). The nonlinear horizontal perturbation terms will be neglected because they do not vary on a tidal timescale, and their uncertainty is about the same magnitude as the terms themselves. The vertical acceleration term cannot be accurately quantified due to error in the

Table 2
Momentum Budget Terms: Statistics (m/s^2)

Momentum budget term	12mN mean	12mN standard deviation	12mS mean	12mS standard deviation
$\frac{\partial U}{\partial t}$	1.06×10^{-7}	3.16×10^{-5}	8.69×10^{-8}	3.64×10^{-5}
$\int_0^1 v \frac{\partial u}{\partial y}$	2.79×10^{-6}	9.24×10^{-6}		
$\int_0^1 u \frac{\partial u}{\partial x}$	-1.17×10^{-5}	1.68×10^{-5}	-1.17×10^{-5}	1.68×10^{-5}
$-g \frac{\partial \eta}{\partial x}$		3.63×10^{-5}		3.63×10^{-5}
$\frac{1}{\rho_0 D} \tau_b$	-7.98×10^{-6}	2.75×10^{-5}	-4.75×10^{-6}	1.06×10^{-5}
$\frac{1}{\rho_0 D} \tau_s$	-4.40×10^{-7}	1.14×10^{-6}	-4.40×10^{-7}	1.14×10^{-6}
fV	4.23×10^{-7}	8.74×10^{-7}	3.25×10^{-7}	9.23×10^{-7}
$\frac{\sigma}{D} \left(\int_0^1 \frac{\partial u_j}{\partial \sigma} \left(u_j \frac{\partial D}{\partial x_j} + \frac{\partial D}{\partial t} \right) d\sigma \right)$	1.68×10^{-6}	2.34×10^{-6}	1.68×10^{-6}	2.34×10^{-6}

Note. A cross-shelf advective acceleration could not be calculated for the 12mS mooring. Per the definition of the sea surface displacement (Section 3), the mean barotropic pressure gradient is defined to be zero.

vertical velocity measurement, but this term can be expected to be small, based on scaling considerations. Further, we cannot properly calculate the baroclinic terms because of the absence of a thermistor chain at the 12mS mooring. However, given that an instrument tower situated $\sim$ 56 m south of the 12mN mooring, in the alongshore direction, carried three additional thermistors at 0.37, 1.2, and 2.4 mab, at least one of the baroclinic terms in equation (4) can be roughly estimated. Assuming that D remains the same between the 12mN thermistor chain and the instrument tower, and assuming that any density above 2.4 mab is constant at the instrument tower, thus resulting in an overestimate of horizontal density gradients,

$$\frac{gD}{\rho_0} \frac{\partial}{\partial x_i} \int_0^1 \int_\sigma^1 \rho \, d\sigma \sim O\left(10^{-6}\right), \tag{10}$$

an order of magnitude smaller than the dominant terms. The statistics for the terms that could be fully quantified are displayed in Table 2.

The variability of the momentum budget terms (numbered in equation (4)) is best examined as a function of tidal phase. We use the depth-averaged alongshore velocity to determine the M_2 phase, with the interval between velocity peaks defining one full tidal oscillation (Figure 3e). The tidal phase is labeled as $\phi = \pi \frac{\Delta t}{T}$ for instances corresponding to a velocity accelerating in the southward direction and $\phi = \pi \frac{\Delta t}{T} + \pi$ for velocities accelerating in the northward direction, where Δt is the time difference between the data and the previous maximum/minimum in the velocity, and T is the time elapsed between subsequent maxima and minima (i.e., the duration of one tidal oscillation). At every tidal oscillation, $\frac{|U|}{|U|_{\max}} > 0.25$, where $|U|$ is the velocity range and $|U|_{\max}$ is the maximum over the entire time series. In total, 42 tidal cycles were observed.

Although the sea surface displacement (η) generally serves as a good marker of tidal phase in unstratified environments, in this case, η is incoherent with the momentum budget terms. For example, the pressure gradient and η show a coherence squared (Coh^2) of Coh$^2 = 0.55$ at the semidiurnal frequency, while the pressure gradient and U are almost perfectly coherent (Coh$^2 = 0.99$) at that same frequency. We argue here that the nearshore pressure gradient and the alongshore velocities are driven primarily by the internal tide, while the observed surface displacement is dominated by the barotropic tide. This will be revisited in section 5.

As shown in Figure 5a, throughout a tidal oscillation, the pressure and the alongshore depth-averaged velocity are in quadrature; the maximum correlation ($r = 0.56$) between both occurs when the velocity leads the sea surface height signal by 3.5 hr, around a fourth of the M_2 tidal cycle. Further, we observe a large scatter in the displacement η, given its incoherence with the depth-averaged alongshore velocity U. The cross-shore velocity is weak and asymmetric throughout a tidal cycle, with smaller magnitudes during the latter half of the cycle.

Following previous studies that neglect the advective acceleration due to instrument limitations or scaling arguments (Fewings & Lentz, 2010; Hickey, 1984; Lentz et al., 1999; Lentz & Raubenheimer, 1999), we first consider phase averages of the momentum budget unsteadiness, barotropic pressure gradient, and bottom drag (Figures 5b and 5c), having excluded the nonlinear inertial terms. Figure 5 also contains the phase-averaged
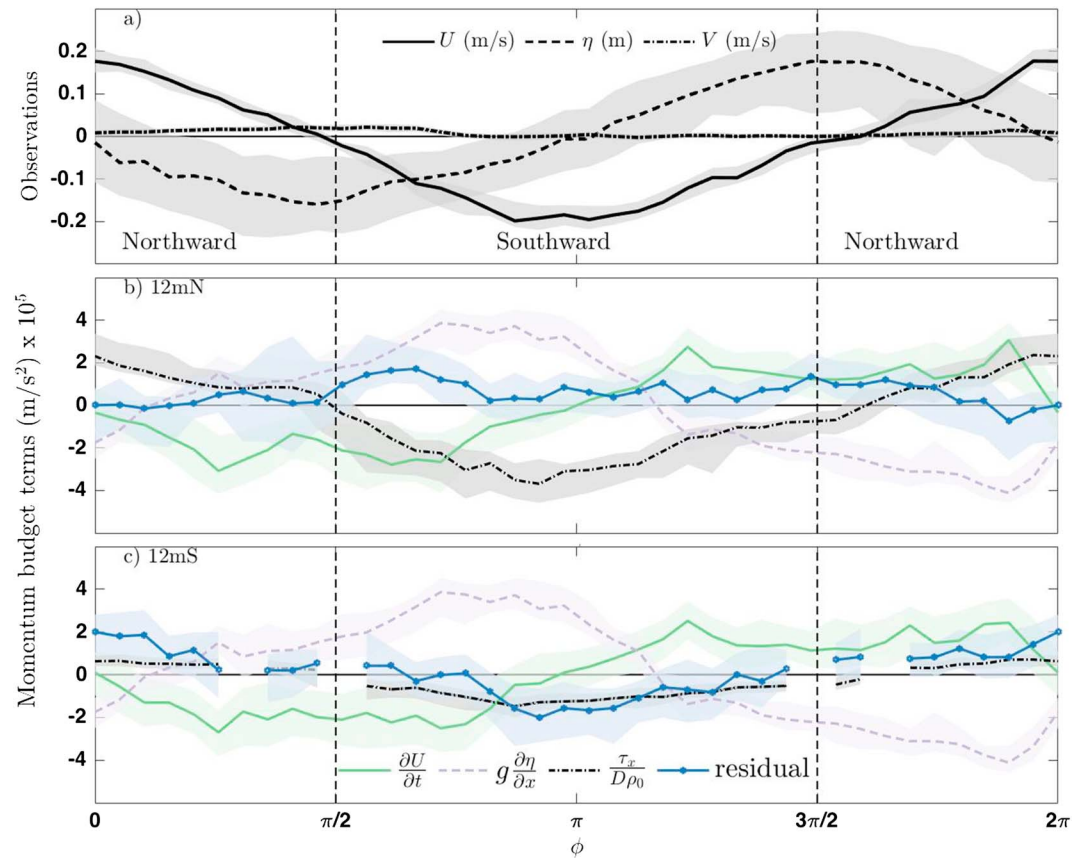
Figure 5. Tidal phase median values of (a) observed variables at 12mN, and estimated momentum budget terms at (b) 12mN and (c) 12mS, with shaded 95% confidence intervals from bootstrapping. Median values calculated from less than 25 valid estimates were not plotted. (The vertical black dashed lines indicate the transition between northward and southward mean flow.)

residual momentum R necessary to close the budget, given as

$$R = -\left(\frac{\partial U_i}{\partial t} + g\frac{\partial \eta}{\partial x_i} + \frac{\tau_b}{D\rho_0} \right). \tag{11}$$

Tidal phase averages of the momentum budget estimates show that unsteadiness and pressure gradient are dominant terms at both 12m moorings (Figures 5b and 5c). These are not in phase; the unsteadiness term is almost negligible when the pressure gradient is at its maximum. Bottom drag also plays a dominant role at 12mN, being of comparable magnitude as the unsteadiness and the pressure gradient, balancing the pressure gradient during almost half of the tidal cycle. The residual (R) at 12mN is near zero: The combination of the three dominant terms is sufficient to close the momentum budget, within uncertainty, during most of the tidal cycle (Figure 5b and Table 3). Although bottom drag at 12mS is weaker (Figure 5c), it offsets some of the barotropic pressure gradient when longshore velocities peak ($\phi \sim 0$, $\phi \sim \pi$). The magnitude of R at 12mS can surpass that of the bottom drag and even exceed that of the unsteadiness when $\phi \sim 0$ and $\phi \sim \pi$ (Figure 5c).

Comparing R at 12mS to our estimated advective acceleration from measurements (term 2 in equation (4)):

$$\int_0^1 u_j \frac{\partial u_i}{\partial x_j} d\sigma \tag{12}$$

shows that the two agree within uncertainty when the depth-averaged alongshore velocity is southward ($\pi/2 < \phi < 3\pi/2$; Figure 6b). However, the observed advective acceleration fails to account for the residual when the currents are northward ($\phi \sim 3\pi/2$ to $\phi \sim \pi/2$; Figure 6b). Further, the smaller residual at 12mN (Figures 5b and 6a) suggests that the advective acceleration as measured between the two sites is not repre-

Table 3
Percentage of the Tidal Cycle When the Momentum Budget Closes Under Different Balances

Balance	Percent closure	
	12mN (%)	12mS (%)
$\frac{\partial U}{\partial t} = -g\frac{\partial \eta}{\partial x}$	27.5	30.0
$\int_0^1 u\frac{\partial u}{\partial x}d\sigma = -g\frac{\partial \eta}{\partial x}$	22.5	22.5
$g\frac{\partial \eta}{\partial x} = -\frac{1}{D\rho_0}\tau_b$	47.5	27.3
$\frac{\partial U}{\partial t} = -g\frac{\partial \eta}{\partial x} - \frac{1}{D\rho_0}\tau_b$	75.0	60.6
$\frac{\partial U}{\partial t} + \int_0^1 u\frac{\partial u}{\partial x}d\sigma = -g\frac{\partial \eta}{\partial x}$	25.0	27.5
$\frac{\partial U}{\partial t} + \int_0^1 v\frac{\partial u}{\partial y}d\sigma = -g\frac{\partial \eta}{\partial x}$	32.5	
$\frac{\partial U}{\partial t} + \int_0^1 u\frac{\partial u}{\partial x}d\sigma = -g\frac{\partial \eta}{\partial x} - \frac{1}{D\rho_0}\tau_b$	25.0	48.4
$\frac{\partial U}{\partial t} + \int_0^1 v\frac{\partial u}{\partial y}d\sigma = -g\frac{\partial \eta}{\partial x} - \frac{1}{D\rho_0}\tau_b$	77.5	
$\frac{\partial U}{\partial t} + \int_0^1 u\frac{\partial u}{\partial x}d\sigma + \int_0^1 v\frac{\partial u}{\partial y}d\sigma = -g\frac{\partial \eta}{\partial x}$	37.5	
$\frac{\partial U}{\partial t} + \int_0^1 u\frac{\partial u}{\partial x}d\sigma + \int_0^1 v\frac{\partial u}{\partial y}d\sigma = -g\frac{\partial \eta}{\partial x} - \frac{1}{D\rho_0}\tau_b$	45.0	
$\frac{\partial U}{\partial t} = -\frac{1}{D\rho_0}\tau_b$	42.5	51.5%
$\frac{\partial U}{\partial t} + \int_0^1 u\frac{\partial u}{\partial x}d\sigma = 0$	25.0	32.5%
$\frac{\partial U}{\partial t} + \int_0^1 u\frac{\partial u}{\partial x}d\sigma = -\frac{1}{D\rho_0}\tau_b$	47.5	45.5%

A cross-shelf advective acceleration could not be calculated for the 12mS mooring.

sentative at the northern site. This is all consistent with local acceleration of flow in the vicinity of the 12mS location for both northward and southward flow, as discussed at the end of this section. Alternatively, the residual in the 12mS momentum budget (Figures 5c and 6b) may be a result of underestimated bottom drag from the log fits. Momentum budget closure can improve at 12mS by increasing the magnitude of the drag by a factor of 2 or 3, if advective acceleration is neglected. Nevertheless, we have likely not underestimated the bottom drag at 12mS, given that the same fitting methods and quality control were applied to the 12mN data and yielded the appropriate results to close the momentum budget at that location. Moreover, as mentioned in section 4.1, the drag estimates at the 12mS mooring were confirmed with additional methods and data. In fact, if we retain the effects of advective acceleration at 12mS, an increase in bottom drag can only improve the momentum balance over part of the cycle, when alongshore velocity is southward, and leads to a larger net residual.

Finally, we can evaluate the role of the different terms in the momentum budget and their contribution to budget closure as a function of tidal phase. We evaluate model closure by estimating the phase-averaged residual in the momentum budget and quantifying the percentage of time that this residual differs from zero, within 95% confidence intervals, when we can consider the momentum budget as effectively closed. Statistics are summarized in Table 3.

A simple balance between the unsteady term and the barotropic pressure gradient,

$$\frac{\partial U_i}{\partial t} = -g\frac{\partial \eta}{\partial x_i}, \tag{13}$$

leads to phase-averaged momentum budget closure during 27–30% of a tidal cycle at both 12m moorings; this unsteady balance suggests that the frictional timescale for the alongshore flow on the inner shelf is comparable to the tidal timescale. Adding the bottom drag improves the closure of the budget dramatically (75% and 61% closure at 12mN and 12mS, respectively) since the term plays an important role in balancing the barotropic pressure gradient. The difference in percentage closure between mooring locations for this three-term closure (including unsteadiness, barotropic pressure gradient, and bottom drag) is not statistically significant due to the small number of degrees of freedom (tidal phase bins). Note that including the cross-shore advective acceleration (Figure 6a) in the previous balance of unsteadiness, pressure gradient and bottom drag increases the percentage of closure at 12mN to 78% of the tidal cycle.
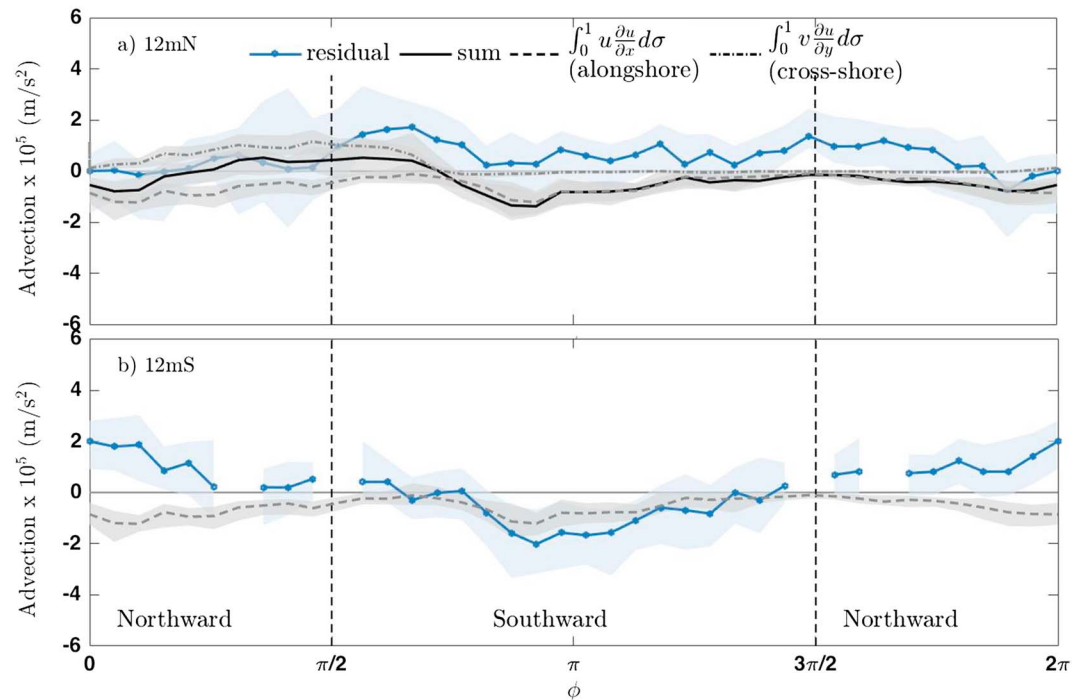
Figure 6. Tidal phase median values from the estimated total and individual components of the advective acceleration, as compared to the momentum budget residual, with shaded 95% confidence intervals from bootstrapping for (a) 12mN and (b) 12mS. Median values calculated from less than 25 valid estimates were not plotted. There is no estimate for the cross-shore advective acceleration at the 12mS site, so this term (and the sum of the terms) has been omitted from the lower plot.

Although the alongshore advective acceleration does not improve the closure at 12mN, it is an important term at the 12mS mooring, as discussed above; in fact, the residual and the alongshore advective acceleration match, within uncertainties, when the velocities flow southward (Figure 6b). A budget at 12mS that includes the unsteadiness, bottom drag, alongshore advective acceleration, and barotropic pressure gradient closes 48% of the time. The percentage of net closure is limited because inclusion of the alongshore advective acceleration leads to excess momentum during northward flow. Table 3 shows the full balances and their percentage of closures throughout a tidal cycle.

The excess momentum noted above could be accounted for by a local acceleration at 12mS. For northward flow, a local acceleration at 12mS would require a positive gradient to the south of the site, with a negative gradient to the north, between 12mS and 12mN; for southward flow, the excess momentum at 12mS requires a negative velocity gradient between the two 12m sites. The latter is consistent with the observations, resulting in advective acceleration estimates that do account for the residual in the 12mS momentum budget, while resolution of a gradient to the south of 12mS would require measurements at a third site. This emphasizes the importance of understanding the impacts of the discretization necessary for calculating momentum budgets in the field and the influence of spatial offsets when estimating different terms. This issue of fully estimating the advective acceleration also highlights an important limitation of this study; a denser instrument array is needed to better constrain the advective acceleration terms in the momentum budget. Similar research with instrumentation that can capture dynamics that are important on length scales shorter than $x \sim 250$ m (the alongshore distance between the 12mN and 12mS moorings), such as local advective acceleration, would be valuable to fully assess the importance of these terms.

5. Discussion

The tidal momentum balance, developed here for the fore-reef region, is important in establishing the dominant forcing terms on a semidiurnal timescale. Of particular note is the importance of the bottom drag and the advective acceleration. The alongshore momentum budget at both sites reflects a combination of the momentum balance for a shallow-water wave (unsteadiness $\sim$ pressure gradient) along with the pres-

sure/drag balance that is more commonly associated with shallow tropical reef flats (Hench et al., 2008; Lowe et al., 2009a; Lowe et al., 2010; Monismith, 2014; Rogers et al., 2018). There is an additional, albeit small, influence of the cross-shore advective acceleration term. On the other hand, the alongshore tidal budget at 12mS suggests that advective acceleration is an equally important contributor to the momentum budget as the bottom drag, similar to what Rogers et al. (2015) found over a spur and groove formation on the fore-reef. We hypothesize that the imbalance at the 12mS mooring is associated with a local acceleration of the flow. A close examination of the bathymetry, along with in situ diver observations, indicates that there is a large (~3 m) step 20–30 m to the south of the mooring site, that may play a role in this acceleration. This would explain why the alongshore advective acceleration term is not necessary for the 12mN momentum budget, while it is necessary for the 12mS budget. It also explains why, given our location for the advective acceleration estimate, it only contributes to closing the budget for one flow direction (southward). Our observations of stronger alongshore velocities at 12mS (compared to alongshore velocities at 12mN) agree with this hypothesis of local acceleration.

Following Kumar et al. (2015), the relative importance of the advective acceleration to the bottom drag is highlighted by some elementary scaling analysis, using values from the 12mS mooring. The ratio of these two terms is roughly written as

$$p = \frac{U_j}{U_i} \frac{D\Delta U_i}{U_i C_D \Delta x_j}, \tag{14}$$

where $i, j = 1, 2$, U_i is a characteristic depth-averaged velocity, C_D is the drag coefficient, D is depth, and ΔU_i is the horizontal difference in depth-averaged velocity. Consider, the ratio of the alongshore advective acceleration to the bottom drag, using the standard deviations of the velocities as their characteristic magnitude. From our data at 12mS, $|\Delta U| \sim 0.029$ m/s and oscillates on a semidiurnal cycle, 180° out of phase with the depth-averaged velocity, suggesting convergence or divergence in the alongshore direction. Given $\Delta x = 257.5$ m, $U \sim 0.16$ m/s, $D \sim 12$ m, and $C_D \sim 0.0023$, the ratio of the alongshore advective acceleration to the bottom drag is $p = 3.7$, indicating that these are, roughly, of similar importance. This suggests that the advective acceleration could play an important role in reef environments with highly variable bathymetry.

As previously mentioned, the tidal phase averages were taken to follow the phase of the alongshore velocity (U), instead of the phase of the sea surface displacement (η), since the momentum budget terms have a much clearer coherence with the former. This suggests that internal tides may be playing a role in modifying the alongshore pressure gradient in the nearshore region. Oahu is in a region of intense internal tide activity. Using the Princeton Ocean Model, Carter et al. (2008) estimate that 85% of the semidiurnal barotropic tidal energy lost over the Hawaiian Ridge is converted into internal tides. The energy flux of the semidiurnal internal tide is an order of magnitude larger than that of the diurnal internal tide (Smith et al., 2017). Specifically, given that our study site is near Kaena Ridge, observed to generate intense internal tides (Nash et al., 2006), it is likely that the measured pressure gradients and the resulting velocities are primarily driven by the evanescent tail of the M_2 internal tide propagating in deeper stratified waters offshore, which influences the nearshore region, despite the lack of local stratification. Similar internal tidal currents have been previously observed at other unstratified locations in Hawai'i (Smith et al., 2016).

The bottom drag plays a significant role in this momentum budget, particularly at 12mN, but the drag coefficients estimated here (median drag coefficients of $C_D = 0.0080$ [−0.002, +0.004] and $C_D = 0.0023$ [−0.0006, +0.0009] at 12mN and 12mS, respectively) are on the lower end of those previously reported for tropical coral reefs. According to a summary of C_D estimates provided by Rosman and Hench (2011), results from a variety of studies initially show drag coefficients ranging from $C_D = 0.009$ to $C_D = 0.8$. After converting the various formulations of C_D to a common definition, Rosman and Hench (2011) constrain this range to $C_D = 0.01$–0.12, closer to our estimates for the 12mN mooring. Some of the variability in C_D in the literature may be attributed to the depth dependence of C_D (Lentz et al., 2017; McDonald et al., 2006). Higher drag coefficient are reported in shallower environments, such as in Coronado et al. (2007; $C_D = 0.015$ when $D \sim 5$ m), Lentz et al. (2016; $C_D = 0.03$ when $D \sim 1.2$ m), Lowe et al. (2009a; $0.01 < C_D < 0.03$ in a reef-lagoon system), and Rogers et al. (2018; $C_D \sim O(0.01) - O(0.1)$ when $D \sim 1$–3m). However, if there is a large depth to hydrodynamic roughness ratio ($\frac{D}{z_0} > 100$, where z_0 is the hydrodynamic roughness) and a large depth to coral

roughness ratio ($\frac{D}{h} > 10$, where h is the coral roughness), then $C_D \rightarrow 0.01$ (Lentz et al., 2017; McDonald et al., 2006). This may account for why the median C_D at 12mN is comparable to values estimated by Reidenbach et al. (2006; $0.009 < C_D < 0.016$) in the fore-reef region, despite much larger roughness for the latter case (mean roughness of 20 cm with a 16-cm standard deviation). As in Reidenbach et al. (2006), both conditions $\left(\frac{D}{z_0} > 100, \frac{D}{h} > 10 \right)$ are met at our study site, though our roughness estimates have large uncertainties and variability.

On the other hand, the phase-averaged C_D values calculated for our 12mS mooring differ from the estimated $C_D \approx 0.01$ for $\frac{D}{z_0} > 100$, given $\frac{D}{h} > 10$ (Lentz et al., 2017; McDonald et al., 2006); they are, instead, comparable to Reidenbach et al., 2006's (2006) estimate for a sandy bottom ($0.002 < C_D < 0.004$)and the canonical C_D for a sandy bed (Monismith, 2007). Wave spectra at both locations were nearly identical; the difference in drag between our northern and southern moorings is probably related to local differences in the physical roughness between sites, rather than an increase in the apparent roughness of the environment (Grant & Madsen, 1979).

6. Summary

The tidal momentum balances estimated here show the relevant forcing terms that dominate across a semidiurnal cycle at two different alongshore locations on the 12-m isobath of a fore-reef. Although the moorings are in an unstratified environment, coherence analyses suggest that the internal tide plays a role in setting the phase of the momentum budget terms. At the northernmost location, where no sharp changes in bathymetry were observed, the momentum balance is between the unsteadiness, pressure gradient, and bottom drag term. However, at the southernmost mooring, situated near a bathymetric step, the alongshore advective acceleration plays a comparable role to the bottom stress. At both locations, drag coefficients are $O\left(10^{-3}\right)$. The alongshore analysis presented here is of particular interest in adding to more extensive research on cross-shore momentum budgets over coral reefs. Particularly, the importance of the alongshore advective acceleration at the 12mS mooring suggests that variations in bathymetry, like those associated with spur and groove formations, can have consequences for alongshore physical and biological dispersion (e.g., sediments, pollutants, and larvae).

Appendix A: Log Fits

For each time step, successive nonlinear fits with incremental depths are applied to non-interpolated velocity profiles to find the four parameters in equation (8). At a time t_i, a fit is done from the first bin (at $z \sim 1$ mab) to $z \sim 0.25D$, where D is the water depth. Then, the fit at t_i is repeated a number of times, each time adding an extra bin to the fit, until the last bin in the fit reaches $z = 0.40D$. The ADCP bins are considered to be independent, although some overlap is expected, since the length of the transmit pulse (0.37 m) is larger than the bin size (0.25 m). If $Ri > 0.25$ anywhere in the velocity profile, the fit is invalidated. The boundary layer thickness (δ) is defined as the highest bin in each fit. Of all the fits corresponding to t_i, only the one with the largest R^2 is saved, and it is only used in this analysis if $R^2 > 0.95$. The process is repeated three times at each location, using alongshore velocities with their associated instrument error (Appendix B) being (1) added, (2) subtracted, or (3) neglected.

Appendix B: Uncertainty Calculations

Any term F in our analysis that is a function of independent variables χ_i has an uncertainty σ_F calculated according to error propagation

$$\sigma_F^2 = \sum_{i=1}^{N} \left(\frac{\partial F}{\partial \chi_i} \sigma_\chi \right)^2 . \tag{B1}$$

The first type of uncertainty accounted for is instrument error. In particular, the uncertainty in ADCP velocities comes from long-term instrument accuracy ($\sigma_{long} \sim 0.0025$ m/s), heading and motion errors ($\sigma_{head} \sim 0.0005$ m/s), and statistical uncertainty after averaging pings ($\sigma_{stat} \sim 0.0014$ m/s). In total, the ADCP velocity error is $\sigma_u \sim 0.005$ m/s, before depth averaging. The uncertainty in the ADCP time stamp ($\sigma_{time} \sim 0.01$ s), as well as from pitch and roll, is taken from Giddings et al. (2014). The uncertainty in depth calculations is equal

to that from the ADCP pressure sensor (0.1 % of the total pressure). The uncertainty in the pressure gradient stems from the error in the quartz pressure sensors (0.01 % of the total pressure).

To compute the uncertainty in the median momentum budget terms along a tidal cycle (Figure 5), phase averaging was performed three different ways: (1) using the terms with no uncertainty, (2) using the terms with the upper uncertainty limit applied, and (3) using the terms with the lower uncertainty limit applied. As part of the phase averaging, the median is calculated from each of those three iterations, and we assign a 95% confidence interval from bootstrapping (with $n = 10,000$ random samplings). Figures 5 and 6 show the medians corresponding to the phase averaging performed using data without uncertainty. However, the lower and upper bounds for the confidence intervals come from taking the minimum and maximum bootstrap uncertainty, respectively, in all three of the iterations previously described. The confidence intervals for the phase-averaged momentum budget terms are, presumably, conservative estimates of the true uncertainty. Error stemming from the GPS locations, rotations to the along and cross-shore axes, or interpolations/extrapolations is not accounted for.

Appendix C: Additional Log Fit Statistics

In order to provide full statistics of the log fit parameters, we include here a table of mean values, with their 95% confidence intervals.

Table C1
Mean Values of Log Fit Parameters Taken From the Entire Time Series

	12mN	12mS
Percent with $R^2 \geq 0.95$	72%	53%
u_* (m/s)	0.016 ± 0.002	0.01 ± 0.0012
z_0 (m)	0.17 ± 0.05	$0.028\ [-0.01, +0.02]$
z_{ref} (m)	$0.029\ [-0.02 + 0.002]$	$0.0018\ [-0.0006, +0.003]$
δ (m)	$3.80\ [-0.03, +0.04]$	$3.68\ [-0.03, +0.04]$
C_D	$0.0086\ [-0.003, +0.01]$	$0.0032\ [-0.001, +0.002]$
C_D^+	$0.0076\ [-0.003, +0.006]$	$0.0035\ [-0.002, +0.005]$
C_D^-	$0.0094\ [-0.003, +0.02]$	$0.0030\ [-0.0008, +0.001]$

Note. The asymmetric confidence intervals result from using bootstrap methods.
[+] Drag coefficients calculated using positive alongshore, depth-averaged velocities.
[−] Drag coefficients calculated using negative alongshore, depth-averaged velocities.

References

Arzeno, I. B., Collignon, A., Merrifield, M., Giddings, S. N., & Pawlak, G. (2018). Oceanographic data taken over a fringing coral reef near Makua Beach, Oahu, Hawai'i (2013). UC San Diego Library Digital Collections, https://doi.org/10.6075/J09G5K1F

Black, K. P. (1993). The relative importance of local retention and inter-reef dispersal of neutrally buoyant material on coral reefs. *Coral reefs*, *12*, 43–53.

Carter, G. S., Merrifield, M. A., Becker, J. M., Katsumata, K., Gregg, M. C., Luther, D. S., et al. (2008). Energetics of M$_2$ barotropic-to-baroclinic tidal conversion at the Hawaiian Islands. *Journal of Physical Oceanography*, *381*, 2205–2223. https://doi.org/10.1175/2008JPO3860.1

Coles, D. (1956). The law of the wake in the turbulent boundary layer. *Journal of Fluid Mechanics*, *1*(2), 191–226. https://doi.org/10.1017/S0022112056000135

Coronado, C., Candela, J., Iglesias-Prieto, R., Sheinbaum, J., López, M., & Ocampo-Torres, F. J. (2007). On the circulation in the Puerto Morelos fringing reef lagoon. *Coral Reefs*, *26*, 149–163. https://doi.org/10.1007/s00338-006-0175-9

Cowen, R. K., Lwiza, K. M., Sponaugle, S., Paris, C. B., & Olson, D. B. (2000). Connectivity of marine population: Open or closed? *Science*, *287*, 857–859. https://doi.org/10.1126/science.287.5454.857

Douillet, P., Ouillon, S., & Cordier, E. (2001). A numerical model for fine suspended sediment transport in the southwest lagoon of New Caledonia. *Coral Reefs*, *20*, 361–372. https://doi.org/10.1007/s00338-001-0193-6

Fewings, M. R., & Lentz, S. J. (2010). Momentum balances on the inner continental shelf at Martha's Vineyard Coastal Observatory. *Journal of Geophysical Research*, *115*, C12023. https://doi.org/10.1029/2009JC005578

Gerbi, G. P., Trowbridge, J. H., Edson, J. B., Plueddemann, A. J., Terray, E. A., & Fredericks, J. J. (2008). Measurements of momentum and heat transfer across the air-sea interface. *Journal of Physical Oceanography*, *38*(5), 1054–1072. https://doi.org/10.1175/2007JPO3739.1

Giddings, S. N., Monismith, S. G., Fong, D. A., & Stacey, M. T. (2014). Using depth-normalized coordinates to examine mass transport residual circulation in estuaries with large tidal amplitude relative to the mean depth. *Journal of Physical Oceanography*, *44*, 128–148. https://doi.org/10.1175/JPO-D-12-0201.1

Gilg, M. R., & Hilbish, T. J. (2003). The geography of marine larval dispersal: Coupling genetics with fine-scale physical oceanography. *Ecology*, *84*, 2989–2998. https://doi.org/10.1890/02-0498

Grant, W. D., & Madsen, O. S. (1979). Combined wave and current interaction with a rough bottom. *Journal of Geophysical Research*, *84*, 1797–1808. https://doi.org/10.1029/JC084iC04p01797

Grant, W. D., & Madsen, O. S. (1986). The continental shelf bottom boundary layer. *Annual Review of Fluid Mechanics*, *18*, 265–305. https://doi.org/10.1146/annurev.fl.18.010186.001405

Green, A. L., Maypa, A. P., Almany, G. R., Rhodes, K. L., Weeks, R., Abesamis, R. A, et al. (2015). Larval dispersal and movement patterns of coral reef fishes, and implications for marine reserve network design. *Biological Reviews*, *90*, 1215–1247. https://doi.org/10.1111/brv.12155

Hench, J. L., Leichter, J. J., & Monismith, S. G. (2008). Episodic circulation and exchange in a wave–driven coral reef and lagoon system. *Limnology and Oceanography*, *53*, 2681–2694. https://doi.org/10.4319/lo.2008.53.6.2681

Hickey, B. M. (1984). The fluctuating longshore pressure gradient on the Pacific Northwest Shelf: A dynamical analysis. *Journal of Physical Oceanography*, *14*, 276–293. https://doi.org/10.1175/1520-0485(1984)014<0276:TFLPGO>2.0.CO;2

Hitzl, D. E., Chen, Y. L., & Van Nguyen, H. (2014). Numerical simulations and observations of airflow through the 'Alenuihāhā Channel, Hawaii. *Monthly Weather Review*, *142*, 4696–4718. https://doi.org/10.1175/MWR-D-13-00312.1

Jaramillo, S., & Pawlak, G. (2011). AUV-based bed roughness mapping over a tropical reef. *Coral Reefs*, *30*, 11–23. https://doi.org/10.1007/s00338-011-0731-9

Kirincich, A. R., Lentz, S. J., & Gerbi, G. P. (2010). Calculating Reynolds stresses from ADCP measurements in the presence of surface gravity waves using the cospectra-fit method. *Journal of Atmospheric and Oceanic Technology*, *27*(5), 889–907. https://doi.org/10.1175/2009JTECHO682.1

Kirincich, A. R., & Rosman, J. H. (2011). A comparison of methods for estimating Reynolds stress from ADCP measurements in wavy environments. *Journal of Atmospheric and Oceanic Technology*, *28*(11), 1539–1553. https://doi.org/10.1175/JTECH-D-11-00001.1

Kitheka, J. U. (1997). Coastal tidally-driven circulation and the role of water exchange in the linkage between tropical coastal ecosystem. *Estuarine, Coastal and Shelf Science*, *45*, 177–187. https://doi.org/10.1006/ecss.1996.0189

Kumar, N., Feddersen, F., Uchiyama, Y., McWilliams, J., & O'Reilly, W. (2015). Midshelf to surfzone coupled ROMS-SWAN model data comparison of waves, currents, and temperature: Diagnosis of subtidal forcings and response. *Journal of Physical Oceanography*, *45*, 1464–1490. https://doi.org/10.1175/JPO-D-14-0151.1

Lentz, S. J., Churchill, J. H., & Davis, K. A. (2018). Coral reef drag coefficients—Surface gravity wave enhancement. *Journal of Physical Oceanography*, *48*, 1555–1566. https://doi.org/10.1175/JPO-D-17-0231.1

Lentz, S. J., Churchill, J. H., Davis, K. A., Farrar, J. T., Pineda, J., & Starczak, V. (2016). The characteristics and dynamics of wave-driven flow across a platform coral reef in the Red Sea. *Journal of Geophysical Research: Oceans*, *121*, 1360–1376. https://doi.org/10.1002/2015JC011141

Lentz, S. J., Davis, K. A., Churchill, J. H., & DeCarlo, T. M. (2017). Coral reef drag coefficients—Water depth dependence. *Journal of Physical Oceanography*, *47*, 1061–1075. https://doi.org/10.1175/JPO-D-16-0248.1

Lentz, S., Guza, R. T., Elgar, S., Feddersen, F., & Herbers, T. H. C. (1999). Momentum balances on the North Carolina inner shelf. *Journal of Geophysical Research*, *104*, 18205–18226. https://doi.org/10.1029/1999JC900101

Lentz, S. J., & Raubenheimer, B. (1999). Field observations of wave setup. *Journal of Geophysical Research*, *104*, 25867–25875. https://doi.org/10.1029/1999JC900239

Li, L., & Chen, Y. L. (2017). Numerical simulations of two trapped mountain lee waves downstream of Oahu. *Journal of Applied Meteorology and Climatology*, *56*, 1305–1324. https://doi.org/10.1175/JAMC-D-15-0341.1

Lowe, R. J., & Falter, J. L. (2015). Oceanic forcing of coral reefs. *Annual Review of Marine Science*, *7*, 43–66. https://doi.org/10.1146/annurev-marine-010814-015834

Lowe, R. J., Falter, J. L., Monismith, S. G., & Atkinson, M. J. (2009a). Wave-driven circulation of a coastal reef-lagoon system. *Journal of Physical Oceanography*, *39*, 873–893. https://doi.org/10.1175/2008JPO3958.1

Lowe, R. J., Falter, J. L., Monismith, S. G., & Atkinson, M. J. (2009b). A numerical study of circulation in a coastal reef-lagoon system. *Journal of Geophysical Research*, *114*, 997–1015. https://doi.org/10.1029/2008JC005081

Lowe, R. J., Hart, C., & Pattiaratchi, C. B. (2010). Morphological constraints to wave–driven circulation in coastal reef–lagoon systems: A numerical study. *Journal of Geophysical Research*, *115*, 447–460. https://doi.org/10.1029/2009JC005753

McDonald, C. B., Koseff, J. R., & Monismith, S. G. (2006). Effects of the depth to coral height ratio on drag coefficients for unidirectional flow over coral. *Limnology and Oceanography*, *51*, 1294–1301. https://doi.org/10.4319/lo.2006.51.3.1294

Monismith, S. G. (2007). Hydrodynamics of coral reefs. *Annual Review of Fluid Mechanics*, *39*, 37–55. https://doi.org/10.1146/annurev.fluid.38.050304.092125

Monismith, S. G. (2014). Flow through a rough, shallow reef. *Coral Reefs*, *33*, 99–104. https://doi.org/10.1007/s00338-013-1107-0

Nash, J. D., Kunze, E., Lee, C. M., & Sanford, T. B. (2006). Structure of the baroclinic tide generated at Kaena Ridge, Hawaii. *Journal of Physical Oceanography*, *36*, 1123–1135. https://doi.org/10.1175/JPO2883.1

Nezu, I., & Rodi, W. (1986). Open-channel flow measurements with a laser Doppler anemometer. *Journal of Hydraulic Engineering*, *112*(5), 335–355. https://doi.org/10.1061/(ASCE)0733-9429(1986)112:5(335)

Nunes, V., & Pawlak, G. (2008). Observations of bed roughness of a coral reef. *Journal of Coastal Research*, *24*, 39–50. https://doi.org/10.2112/05-0616.1

Reidenbach, M. A., Monismith, S. G., Koseff, J. R., Yahel, G., & Genin, A. (2006). Boundary layer turbulence and flow structure over a fringing coral reef. *Limnology and Oceanography*, *51*, 1956–1968. https://doi.org/10.4319/lo.2006.51.5.1956

Rogers, C. S. (1990). Responses of coral reefs and reef organisms to sedimentation. *Marine Ecology Progress Series*, *62*, 185–202.

Rogers, J. S, Maticka, S. A., Chirayath, V., Woodson, C. B., Alonso, J. J., & Monismith, S. G. (2018). Connecting flow over complex terrain to hydrodynamic roughness on a coral reef. *Journal of Physical Oceanography*, *48*, 1567–1587. https://doi.org/110.1175/JPO-D-18-0013.1

Rogers, J. S., Monismith, S. G., Dunbar, R. B., & Koweek, D. (2015). Field observations of wave-driven circulation over spur and groove formations on a coral reef. *Journal of Geophysical Research: Oceans*, *120*, 145–160. https://doi.org/10.1002/2014JC010464

Rosman, J. H., & Hench, J. L. (2011). A framework for understanding drag parameterizations for coral reefs. *Journal of Geophysical Research*, *116*, C08025. https://doi.org/10.1029/2010JC006892

Smith, S. D. (1988). Coefficients for sea surface wind stress, heat flux, and wind profiles as a function of wind speed and temperature. *Journal of Geophysical Research*, *93*, 15467–15472. https://doi.org/10.1029/JC093iC12p15467

Smith, K. A., Merrifield, M. A., & Carter, G. S. (2017). Coastal-trapped behavior of the diurnal internal tide at O'ahu, Hawai'i. *Journal of Geophysical Research: Oceans*, *122*, 4257–4273. https://doi.org/10.1002/2016JC012436

Smith, K. A., Rocheleau, G., Merrifield, M. A., Jaramillo, S., & Pawlak, G. (2016). Temperature variability caused by internal tides in the coral reef ecosystem of Hanauma bay, Hawai'i. *Continental Shelf Research*, *116*, 1–12. https://doi.org/10.1016/j.csr.2016.01.004

Taebi, S., Lowe, R. J., Pattiaratchi, C. B., Ivey, G. N., Symonds, G., & Brinkman, R. (2011). Nearshore circulation in a tropical fringing reef system. *Journal of Geophysical Research*, *116*, C02016. https://doi.org/10.1029/2010JC006439

Williams, D. M., Wolanski, E., & Andrews, J. C. (1984). Transport mechanisms and the potential movement of planktonic larvae in the central region of the Great Barrier Reef. *Coral Reefs*, *3*, 229–236. https://doi.org/10.1007/BF00288259

Wolanski, E., & Kingsford, M. J. (2014). Oceanographic and behavioural assumptions in models of the fate of coral and coral reef fish larvae. *Journal of The Royal Society Interface*, *11*, 43–66. https://doi.org/10.1098/rsif.2014.0209